



LAWRENCE
LIVERMORE
NATIONAL
LABORATORY

A Grain Boundary Damage Model for Delamination

M. C. Messner, A. J. Beaudoin, R. H. Dodds

January 14, 2015

Computational Mechanics

Disclaimer

This document was prepared as an account of work sponsored by an agency of the United States government. Neither the United States government nor Lawrence Livermore National Security, LLC, nor any of their employees makes any warranty, expressed or implied, or assumes any legal liability or responsibility for the accuracy, completeness, or usefulness of any information, apparatus, product, or process disclosed, or represents that its use would not infringe privately owned rights. Reference herein to any specific commercial product, process, or service by trade name, trademark, manufacturer, or otherwise does not necessarily constitute or imply its endorsement, recommendation, or favoring by the United States government or Lawrence Livermore National Security, LLC. The views and opinions of authors expressed herein do not necessarily state or reflect those of the United States government or Lawrence Livermore National Security, LLC, and shall not be used for advertising or product endorsement purposes.

A grain boundary damage model for delamination

M. C. Messner, A. J. Beaudoin, and R. H. Dodds, Jr.

the date of receipt and acceptance should be inserted later

Abstract Intergranular failure in metallic materials represents a multiscale damage mechanism: some feature of the material microstructure triggers the separation of grain boundaries on the microscale, but the intergranular fractures develop into long cracks on the macroscale. This work develops a multiscale model of grain boundary damage for modeling intergranular delamination – a failure of one particular family of grain boundaries sharing a common normal direction. The key feature of the model is a physically-consistent and mesh independent, multiscale scheme that homogenizes damage at many grain boundaries on the microscale into a single damage parameter on the macroscale to characterize material failure across a plane. The specific application of the damage framework developed here considers delamination failure in modern Al-Li alloys. However, the framework may be readily applied to other metals or composites and to other non-delamination interface geometries – for example, multiple populations of material interfaces with different geometric characteristics.

Keywords Delamination · Intergranular · Aluminum-lithium · Multiscale · Damage

M. C. Messner

Department of Civil and Environmental Engineering, 2113 NCEL MC 250, University of Illinois at Urbana-Champaign, 205 N. Mathews Avenue, Urbana, IL 61801, USA

Currently at Lawrence Livermore National Laboratory, P.O. Box 808, L-227, Livermore, CA 94551, USA

R. H. Dodds, Jr. (✉)

Department of Civil and Environmental Engineering, 2113 NCEL MC 250, University of Illinois at Urbana-Champaign, 205 N. Mathews Avenue, Urbana, IL 61801, USA Tel.: +1-217-320-0034 E-mail: rdodds@illinois.edu

A. J. Beaudoin

Department of Mechanical Science and Engineering, 354 MEB MC 244, University of Illinois at Urbana-Champaign, 1204 Green Street, Urbana, IL 61801, USA

1 Introduction

Intergranular fracture affects many structural metal alloys. Assessment of the safety and reliability of structures susceptible to intergranular failure requires a method to predict the initiation and growth of damage on grain boundaries. Several factors promote crack initiation on grain boundaries:

1. At sufficiently high temperatures the connected network of grain boundaries diffuses lattice vacancies into growing voids [9, 13].
2. The network of grain boundaries accelerates the spread of corrosion and other detrimental environmental factors including hydrogen and radiation [3, 36, 49].
3. During processing, impurities, second phases, and inclusions segregate to the grain boundaries [63].
4. In nanocrystalline materials, grain boundary sliding and partial dislocation motion may initiate cracking [15, 41].
5. The mechanics of the grain interface promotes the plastic growth of voids [37, 39].

Some failure mechanisms overlap more than one category. For example, voids often initiate at inclusions and then grow by creep-induced diffusion [42, 43].

Detailed modeling of intergranular failure in a finite element simulation requires the resolution of each individual grain and a fine discretization near grain boundaries to capture the strains and stresses leading to material separation. As the physical size of the model increases, a detailed discretization of individual grains becomes computationally intractable.

Multiscale methods and homogenization techniques incorporate microstructural information into a macroscale simulation. These methods determine the macroscale response of a point in a continuum from the

response of a representative microstructure for the material at that point [32]. Classical homogenizations treat the macroscale material as a media with undetermined material coefficients to be calculated from microstructural information. Examples include the Voigt [62] and Reuss [45] bounds, self-consistent techniques [40], and Mori-Tanaka methods [50]. These classical homogenizations describe the response of the material by assuming some microstructural geometry – typically ellipsoidal inclusions. Multiscale methods determine the full behavior of a macroscale material point from the microscale response – including the effect of plasticity, microcracking, and detailed microstructural geometry. These methods typically determine the response of the microscale by solving an additional boundary value problem (BVP) over a representative volume element (RVE) and extending the microscale response to the macroscale through a homogenization theory. Frequently, they apply asymptotic homogenization (see, for example [19]), which assumes scale separation and microstructural periodicity. Special techniques, such as the Voroni cell finite element method (VCFEM) by Ghosh and coworkers solve the microscale BVP for a variety of complex microstructures, including damaged RVEs [20–23, 35]. Because each macroscale material point solves the RVE problem, recent work develops efficient microscale solution techniques [16–18] or reduces the complexity of the microscale problem in non-critical regions [24].

This work develops a multiscale model for intergranular damage. A physically based crystal plasticity model simulates the deformation of individual grains on the microscale [34, 38]. A simplified compatibility / equilibrium model, similar to one developed by Evers et al. [14], ties the response of two grains and calculates the intergranular stresses and strains. In turn, this intergranular response drives a microscale damage index representing the degree of grain boundary separation – from a perfect interfacial bond to complete interface separation. Geometric assumptions connect average grain size to element size and homogenize a collection of index values representing intergranular damage into a macroscale measure of damage. The damage model applies this macroscale damage index to the stress/strain response of a conventional, macroscale finite element material model through planar projections – essentially extending the smeared cracking method [44] to nonlinear, large deformation material models. Stiffness degradation methods, *e.g.* the smeared cracking method, have a long history [31] of successfully modeling failure in a wide range of materials from reinforced concrete [44] to sea ice [25]. The homogenization process compares the length scale of the grains to the length scale of the finite element and scales the damage

to failure by the element size to eliminate the mesh dependence of the smeared cracking method (see Bažant and Lin [5]).

While this damage model could represent a variety of intergranular failure mechanisms, this work applies the framework to delamination in Al-Li alloys. Delamination is an intergranular failure mechanism that develops concurrently with the growth of primary, transgranular cracks [11, 54]. Al-Li alloys are lighter, stronger, and generally more fracture resistant than conventional aerospace aluminums, but the difficulty of predicting the development of delaminations hinders their application [47]. Fractography by Richie et al. [55–61, 64] indicates void-growth on grain boundaries triggers delamination failure. Experiments [6, 10, 52] suggest that delamination typically develops along certain favored grain boundaries. These boundaries separate soft/stiff orientation pairs – one grain deforms at low stress with large plastic strains and the neighboring grain deforms at high stress with small plastic strains.

Working with detailed crystal plasticity models of grain boundaries ahead of a long primary crack, our previous work concludes that these soft/stiff grain boundaries develop high mean stresses as a consequence of the interface mechanics of two adjacent single crystal grains – not as a result of any particular material feature [37, 39]. These elevated mean stresses, coupled with large plastic deformations at the boundary, drive void growth, leading to delamination.

Figure 1 shows an image of an EBSD experiment, conducted on a post-delamination M(T) fracture specimen [6]. Different colors in the image indicate different grain orientations. The figure shows a pancake-shaped grain geometry, typical for a rolled, unrecrystallized Al-Li plate. The delamination crack grows intergranularly, occasionally stepping across one wide grain boundary to another. Two directions describe standard experimental configurations – the direction of loading and the direction of primary crack advance. Figure 2 shows these configurations, relative to the standard rolling coordinates. The geometry of delamination divides these six standard configurations into three groups, shown in the figure. Each of the three different groups develops different types of delamination cracks, indicated with thin lines. The different behavior of each configuration results solely from the position of the grains relative to the primary crack – delaminations always develop in the $L - T$ plane, normal to the S -direction.

Based on these observations, the specific implementation of the damage model developed in this work represents microscale, intergranular damage with a damage index based on the Rice-Tracey parameter for plastic void-growth [46]. The bicrystal interface model re-

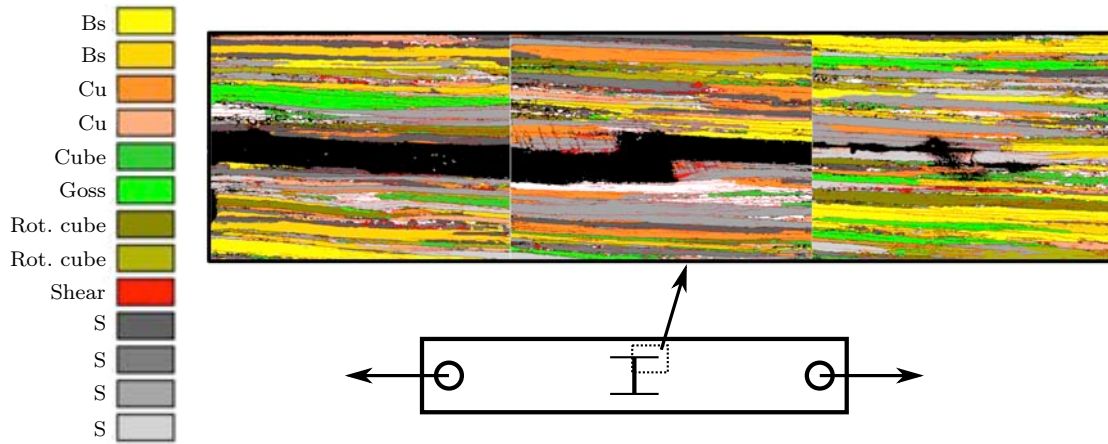


Fig. 1 EBSD image from a fracture test of a M(T) specimen. Image focuses on a single arrestor delamination, extending from the primary crack. Colors indicate different grain orientations. Figure reproduced from Beaudoin et al. [6].

produces the elevated mean stresses and plastic strains that accumulate on soft/stiff Al-Li grain boundaries. The geometric assumptions underlying the damage homogenization treat the grains as laminar stacks of thin, pancake-shaped hexahedra, with separation potentially occurring along planes normal to the S -direction. The damage model reproduces key features of behavior in Al-Li – delamination initiation toughness, growth direction, and interaction with a primary crack. While the particular example provided here represents delamination in Al-Li, the same implementation could also represent other metal alloys that delaminate with similar mechanisms, including 3CR12 and X70 steel [27, 33] and conventional 7000-series aluminums [48]. The framework could also represent intergranular failure in other materials by changing (1) the microscale damage index to represent the physics of the failure mechanism and (2) the geometric assumptions of grain shape and failure plane orientation to match the microstructure of the material.

The presentation here is organized as follows. Section 2 develops the components of the damage model: the compatibility/equilibrium grain boundary model, the Rice-Tracey damage index, the geometric assumptions to homogenize microscale damage to the macroscale, and the projection matrices that apply this damage to a particular failure plane. Section 3 describes verification examples for the grain boundary model and the planar damage projections. Section 4 applies the damage model to study delamination in Al-Li. Section 5 summarizes the conclusions of the work and discusses future developments and applications of the intergranular damage model.

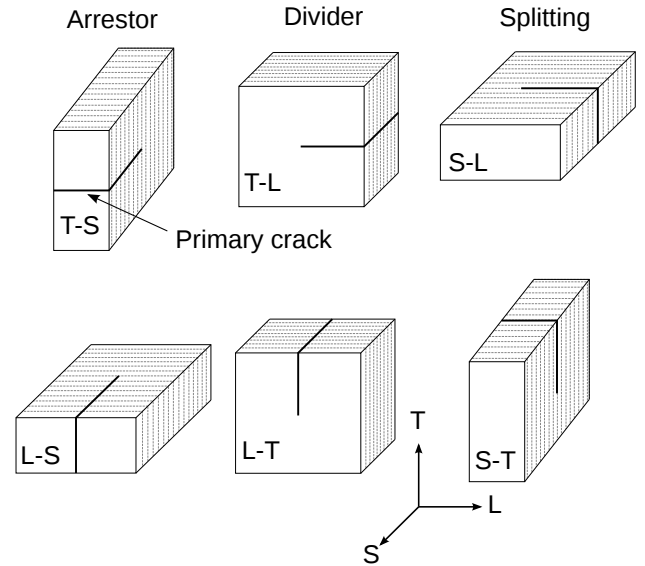


Fig. 2 Standard series of delamination configurations, relative to the standard rolling coordinate system LTS . Fine lines indicate the orientation of elongated $L - T$ grain boundaries.

2 Bicrystal interface damage model

At a minimum, a model for intergranular damage must include the following components:

1. A model to predict the interface stresses along grain boundaries;
2. A damage index to capture the microscale damage mechanism;
3. A homogenization technique connecting microscale and macroscale damage;
4. The macro-constitutive response of the material.

The damage model developed here fulfills each of these requirements:

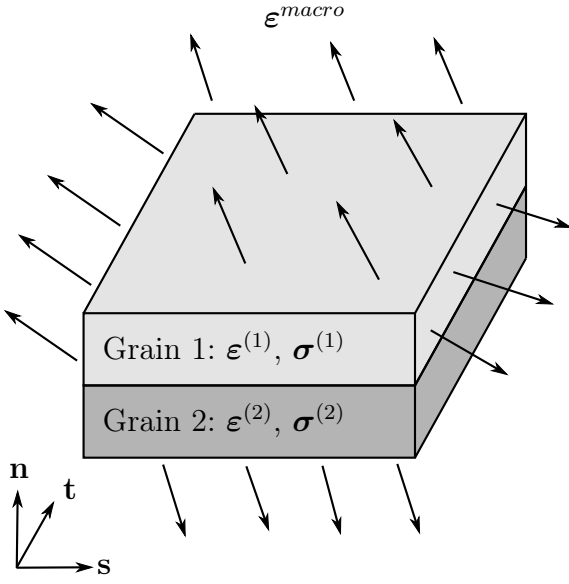


Fig. 3 Bicrystal model – coordinate system normal to the interface plane. The model enforces requirements of stress equilibrium, strain compatibility, and an average Taylor constraint with respect to ϵ^{macro} on the planar interface. Grain constitutive response is simulated with crystal plasticity.

1. An interface model based on strain compatibility and stress equilibrium to predict the development of interface stresses and strains on a bicrystal boundary;
2. A damage index based on the approximate Rice-Tracey parameter to quantify the plastic growth of voids on a grain boundary;
3. A homogenization that translates grain boundary damage on the microscale to planar damage on the macroscale by relating the size of the finite element to the typical grain size of the material;
4. A method for applying *planar* damage to a finite element model.

The following section describes each of these components in detail.

2.1 Grain boundary response

2.1.1 Small strains

Our previous work [37, 39] on Al-Li represents a series of grain boundaries under the loading generated by a long primary crack with detailed crystal plasticity finite element models (CPFEM). These models reveal the development of stresses and plastic strains on the grain boundaries leading to void-growth and delamination cracking. However, they are computationally expensive – requiring thousands of finite elements

per grain and $> 10^6$ of degrees of freedom total. In a previous paper [39], we proposed the outline of a simplified grain boundary model that considers only interface equilibrium and compatibility. Such a model has lower fidelity compared to the detailed CPFEM simulations, but reduces the computational work required to compute the intergranular stresses and strains. This section develops such a reduced model of a grain boundary – a model that considers only the interface of two grains in isolation. The model shares features with a homogenization technique developed by Evers et al. [14], which enforces Hadamard compatibility and stress equilibrium in a large deformation framework. This section adopts a small strain, incremental scheme based on similar compatibility and equilibrium requirements then extends the model to finite strains via the Green-Naghdi [26] objective rate integrated in an unrotated intermediate configuration.

In the interface model, crystal plasticity simulates the constitutive response of individual grains. A previous work [38] describes the details of the adopted crystal plasticity formulation. In small strains, the CP model takes an increment of strain and returns the updated stress. For large strains, the model takes an increment of unrotated strain over $t_n \rightarrow t_{n+1}$ and returns the unrotated Cauchy stress at t_{n+1} . A similar procedure for incremental stress integration requires an incremental interface model. The CP material model also computes the lattice orientation update for each grain and tracks the evolution of internal variables.

Figure 3 illustrates the interface model. The two grains have infinite extent in the boundary plane ($\mathbf{t}-\mathbf{s}$) and zero thickness normal to the boundary interface (\mathbf{n}). The model imposes three conditions on the material response at this idealized, planar interface:

1. Stress equilibrium: $\sigma_{nn}^{(1)} = \sigma_{nn}^{(2)}$, $\sigma_{sn}^{(1)} = \sigma_{sn}^{(2)}$, and $\sigma_{tn}^{(1)} = \sigma_{tn}^{(2)}$.
2. Strain compatibility: $\epsilon_{st}^{(1)} = \epsilon_{st}^{(2)}$, $\epsilon_{tt}^{(1)} = \epsilon_{tt}^{(2)}$, and $\epsilon_{ss}^{(1)} = \epsilon_{ss}^{(2)}$.
3. Average Taylor constraint: $\epsilon^{macro} = \frac{1}{2} (\epsilon^{(1)} + \epsilon^{(2)})$.

These equations describe the constraints in the coordinate system shown in Fig. 3. However, the actual implementation must accommodate interfaces with an arbitrary normal vector and enforce the constraints incrementally.

To handle interfaces of arbitrary orientation, the model takes three orthogonal unit vectors as parameters: \mathbf{n} (normal to the interface) and \mathbf{s} and \mathbf{t} (in the interface plane). The model projects the finite element stress and strain tensors into this coordinate system, performs the stress update, and returns a stress in the original coordinates. Projection matrices carry out these

three operations simultaneously for each constraint. These matrices operate on the Voigt notation equivalents of the symmetric stress and strain tensors. In this form, the constraints are:

1. Stress equilibrium: $\mathbf{P}_{3 \times 6}^e \left(\boldsymbol{\sigma}_{n+1}^{(1)} - \boldsymbol{\sigma}_{n+1}^{(2)} \right)_{6 \times 1} = \mathbf{0}_{3 \times 1}$.
2. Strain compatibility: $\mathbf{P}_{3 \times 6}^e \left(\Delta \boldsymbol{\varepsilon}_{n+1}^{(1)} - \Delta \boldsymbol{\varepsilon}_{n+1}^{(2)} \right)_{6 \times 1} = \mathbf{0}_{3 \times 1}$.
3. Average Taylor constraint: $\left(\Delta \boldsymbol{\varepsilon}_{n+1}^{macro} \right)_{6 \times 1} = \frac{1}{2} \left(\Delta \boldsymbol{\varepsilon}_{n+1}^{(1)} + \Delta \boldsymbol{\varepsilon}_{n+1}^{(2)} \right)_{6 \times 1}$.

The appendix lists the components of the projection tensors $\mathbf{P}_{3 \times 6}^e$ and $\mathbf{P}_{3 \times 6}^c$ in terms of the orthogonal coordinate system ($\mathbf{n}, \mathbf{s}, \mathbf{t}$) and describes the Voigt notation adopted for this work.

The incremental stress update for the crystal plasticity material model is a nonlinear function coupling stress at step $n + 1$ to the strain increment over the step:

$$\begin{aligned} \boldsymbol{\sigma}_{n+1}^{(1)} &= \boldsymbol{\sigma}_{n+1}^{(1)} \left(\Delta \boldsymbol{\varepsilon}_{n+1}^{(1)} \right) \\ \boldsymbol{\sigma}_{n+1}^{(2)} &= \boldsymbol{\sigma}_{n+1}^{(2)} \left(\Delta \boldsymbol{\varepsilon}_{n+1}^{(2)} \right). \end{aligned}$$

The CP material model also provides the consistent linearization of this nonlinear function, the algorithmic tangent:

$$\begin{aligned} \mathbf{A}_{n+1}^{(1)} &= \frac{\partial \boldsymbol{\sigma}_{n+1}^{(1)}}{\partial \Delta \boldsymbol{\varepsilon}_{n+1}^{(1)}} \\ \mathbf{A}_{n+1}^{(2)} &= \frac{\partial \boldsymbol{\sigma}_{n+1}^{(2)}}{\partial \Delta \boldsymbol{\varepsilon}_{n+1}^{(2)}}. \end{aligned}$$

The incremental constraints define a set of nonlinear equations:

$$\begin{aligned} \mathbf{R}_{n+1} &= \begin{bmatrix} \mathbf{P}_{3 \times 6}^e \left(\boldsymbol{\sigma}_{n+1}^{(1)} \left(\Delta \boldsymbol{\varepsilon}_{n+1}^{(1)} \right) - \boldsymbol{\sigma}_{n+1}^{(2)} \left(\Delta \boldsymbol{\varepsilon}_{n+1}^{(2)} \right) \right)_{6 \times 1} \\ \mathbf{P}_{3 \times 6}^c \left(\Delta \boldsymbol{\varepsilon}_{n+1}^{(1)} - \Delta \boldsymbol{\varepsilon}_{n+1}^{(2)} \right)_{6 \times 1} \\ \frac{1}{2} \left(\Delta \boldsymbol{\varepsilon}_{n+1}^{(1)} + \Delta \boldsymbol{\varepsilon}_{n+1}^{(2)} \right)_{6 \times 1} - \left(\Delta \boldsymbol{\varepsilon}_{n+1}^{macro} \right)_{6 \times 1} \end{bmatrix}_{12 \times 1} \\ &= \mathbf{0}_{12 \times 1}. \quad (1) \end{aligned}$$

The Jacobian of this system with respect to the vector of unknowns:

$$\mathbf{x}_{n+1} = \begin{bmatrix} \left(\Delta \boldsymbol{\varepsilon}_{n+1}^{(1)} \right)_{6 \times 1} \\ \left(\Delta \boldsymbol{\varepsilon}_{n+1}^{(2)} \right)_{6 \times 1} \end{bmatrix}_{12 \times 1}$$

is:

$$\mathbf{J}_{n+1} = \begin{bmatrix} \left(\mathbf{P}_{3 \times 6}^e \mathbf{A}_{n+1}^{(1)} \right)_{3 \times 6} & - \left(\mathbf{P}_{3 \times 6}^e \mathbf{A}_{n+1}^{(2)} \right)_{3 \times 6} \\ \left(\mathbf{P}_{3 \times 6}^c \mathbf{I}_{6 \times 6} \right)_{3 \times 6} & - \left(\mathbf{P}_{3 \times 6}^c \mathbf{I}_{6 \times 6} \right)_{3 \times 6} \\ \frac{1}{2} \mathbf{I}_{6 \times 6} & \frac{1}{2} \mathbf{I}_{6 \times 6} \end{bmatrix}_{12 \times 12}. \quad (2)$$

The Newton-Raphson method solves the residual system defined in Eq. 1 using the Jacobian in Eq. 2. Algorithm 1 describes the complete process. A standard Newton-Raphson algorithm often diverges – a backtracking line search parameter improves convergence of the solution. A converged solution typically requires fewer than 10 iterations. The model takes an increment of strain on the macroscale ($\Delta \boldsymbol{\varepsilon}_{n+1}^{macro}$) and finds the microscale bicrystal strain increments $\Delta \boldsymbol{\varepsilon}_{n+1}^{(1)}$ and $\Delta \boldsymbol{\varepsilon}_{n+1}^{(2)}$ that satisfy the three requirements. In the process of computing these strains, the model also finds the updated bicrystal stresses $\boldsymbol{\sigma}_{n+1}^{(1)}$ and $\boldsymbol{\sigma}_{n+1}^{(2)}$ and the associated state variables.

Compared to detailed finite element models of individual grains, this interface model reduces greatly the computational effort required to simulate the response of a bicrystal. Updating of the response for a single bicrystal pair thus requires the solution of a system of 12, coupled nonlinear equations – much less computationally expensive than solving a finite element model resolving the grain behavior, which might contain thousands of elements. Disadvantages of this reduced model are the simplifying assumptions, which neglect: (1) the bulk response of the grains, (2) boundary effects, (3) the influence of more than one neighboring grain, (4) the effects of non-planar grain boundaries, (5) and triple points.

2.1.2 Large strains and lattice rotations

The CP material model tracks the rotation of the crystal lattice with an exponential integrator to maintain orthogonality of the elastic rotation tensor [38]. In large deformations, the CP material model works with increments of corotational strain:

$$\Delta \mathbf{d}_{n+1} = \mathbf{R}_{n+1}^T \Delta \mathbf{D}_{n+1} \mathbf{R}_{n+1}$$

and corotational Cauchy stress:

$$\mathbf{t}_{n+1} = \mathbf{R}_{n+1}^T \boldsymbol{\sigma}_{n+1} \mathbf{R}_{n+1}$$

with $\Delta \mathbf{D}_{n+1} = \mathbf{D}_{n+1} \Delta t_{n+1}$, the integrated deformation rate tensor, and \mathbf{R}_{n+1} the total rotational component of the deformation gradient $\mathbf{F}_{n+1} = \mathbf{R}_{n+1} \mathbf{U}_{n+1}$.

Algorithm 1 The interface compatibility/equilibrium model.

Input: $\Delta\epsilon_{n+1}^{macro}$, crystal states at time t_n .

Form the unknown vector $\mathbf{x}_{n+1}^{(0)} = \begin{bmatrix} \Delta\epsilon_n^{(1)} \\ \Delta\epsilon_n^{(2)} \end{bmatrix}$.

Compute $\mathbf{R}_{n+1}^{(0)}$

While $\|\mathbf{R}_{n+1}^{(i)}\| > \text{tol}$:

 Compute the Jacobian $\mathbf{J}_{n+1}^{(i)}$ with Eq. 2.

 Solve the system $-\mathbf{J}_{n+1}^{(i)}\Delta\mathbf{x}_{n+1}^{(i)} = \mathbf{R}_{n+1}^{(i)}$.

 Update the unknown strains: $\mathbf{x}_{n+1}^{(i+1)} = \mathbf{x}_{n+1}^{(i)} + \Delta\mathbf{x}_{n+1}^{(i)}$

 Compute $\mathbf{R}_{n+1}^{(i+1)}$ with Eq. 1.

 $i + 1 \rightarrow i$

Update the crystal histories to state $n + 1$.

Return the strains $\begin{bmatrix} \Delta\epsilon_{n+1}^{(1)} \\ \Delta\epsilon_{n+1}^{(2)} \end{bmatrix} = \mathbf{x}_{n+1}^{(i+1)}$ and the stresses $\sigma_{n+1}^{(1)}$ and $\sigma_{n+1}^{(2)}$ (computed while calculating $\mathbf{R}_{n+1}^{(i+1)}$).

We assume the orthogonal coordinate system aligned with the boundary evolves with the (total) material point motion:

$$\mathbf{n}_{n+1} = \mathbf{R}_{n+1}\mathbf{n}_0$$

$$\mathbf{s}_{n+1} = \mathbf{R}_{n+1}\mathbf{s}_0$$

$$\mathbf{t}_{n+1} = \mathbf{R}_{n+1}\mathbf{t}_0.$$

With this assumption the equilibrium requirement at large deformations becomes:

$$\begin{aligned} & \left(\sigma_{n+1}^{(1)} - \sigma_{n+1}^{(2)} \right) \cdot \mathbf{n}_{n+1} = \\ & \left(\mathbf{R}_{n+1}\mathbf{t}_{n+1}^{(1)}\mathbf{R}_{n+1}^T - \mathbf{R}_{n+1}\mathbf{t}_{n+1}^{(2)}\mathbf{R}_{n+1}^T \right) \cdot \mathbf{R}_{n+1}\mathbf{n}_{n+1} = \mathbf{0} \end{aligned}$$

$$\mathbf{R}_{n+1} \left(\mathbf{t}_{n+1}^{(1)} - \mathbf{t}_{n+1}^{(2)} \right) \cdot \mathbf{n}_{n+1} = \left(\mathbf{t}_{n+1}^{(1)} - \mathbf{t}_{n+1}^{(2)} \right) \cdot \mathbf{n}_{n+1} = \mathbf{0}.$$

That is, imposition of the equilibrium requirement on the unrotated Cauchy stress is equivalent to imposing equilibrium on the Cauchy stress, provided the boundary normal evolves with the total material rotation. Similar derivations follow for the other two constraints.

Therefore, extending the model described in Section 2.1.1 to large deformations simply requires substituting the unrotated Cauchy stress for the Cauchy stress and the unrotated strain increment for the strain increment. In this form, the model takes an increment of unrotated macroscopic strain and returns the increments of unrotated microscopic strain and the unrotated microscopic stresses. The finite element framework maintains the interpretation of the stresses and strain as corotational quantities and preforms additional rotations as required to convert to the current configuration.

2.2 Damage index based on the Rice-Tracey parameter

Void growth on grain boundaries triggers delamination failure in Al-Li. The interface model in the previous section provides the mechanical response (stresses/strains) on the boundary. This mechanical response drives void-growth – approximated in this work with a damage index based on the Rice-Tracey parameter. The Rice-Tracey parameter [46] is the logarithm of the plastic void-growth ratio of a single void subjected to a mean stress, effective stress, and equivalent plastic strain. The differential equation:

$$\frac{\partial \log(r/r_0)}{\partial \bar{\epsilon}^p} = \exp\left(\frac{1.5\sigma_m}{\sigma_e}\right) \quad (3)$$

$$\log(r/r_0)|_{\bar{\epsilon}^p=0} = 0$$

extends the Rice and Tracey solution to a hardening material [12]. The void-growth ratio does not satisfy the requirement of a continuum damage index, which should vary smoothly from 0 to 1. The present model represents damage with the function:

$$D = \tanh\left(\frac{\log(r/r_0)}{\alpha}\right)$$

with α a material constant. This function does range smoothly from 0 to an asymptote at $D = 1$. The model tracks the damage parameter by evolving the differential equation:

$$\frac{\partial D}{\partial \bar{\epsilon}^p} = \frac{\exp\left(\frac{1.5\sigma_m}{\sigma_e}\right)/\alpha}{\cosh(\log(r/r_0)/\alpha)^2} \quad (4)$$

$$D|_{\bar{\epsilon}^p=0} = 0$$

based on the stresses and plastic strains at a bicrystal interface. Specifically, the model tracks the damage index in each of the two grains at the interface and uses the maximum value from the two grains as the interface damage index. Because the damage function is

asymptotic at $D = 1$, the model cuts off the damage evolution:

$$D_{n+1} = \begin{cases} D_{n+1} & D_{n+1} < D_{cut} \\ 1 & D_{n+1} \geq D_{cut} \end{cases}.$$

In this work, $D_{cut} = 0.95$. This cutoff prevents unnecessary interface stress calculations when a bicrystal pair has separated. After $D = 1$, the model marks the bicrystal as failed and no longer computes stress or damage updates for that particular grain pair.

These equations describe damage evolution either with small strains or with finite strains in the current configuration. At large deformations, the bicrystal interface model returns unrotated stresses and strains, as described above. However, because Eqs. 3 and 4 are functions only of stress and strain invariants, the calculation can occur equivalently in the unrotated configuration (*i.e.* the damage index is rotationally invariant). The process for updating the damage index therefore remains the same for both small and large strains.

The present formulation does not depend on the choice of a specific intergranular damage index. Another damage index, such as the Gurson-Tvergaard-Needleman model [28, 53], could also represent void-growth on the grain boundaries. Furthermore, nothing restricts the formulation to such ductile failure mechanisms. Other damage indexes, driven by the intergranular stresses and strains, could represent intergranular failure.

2.3 Homogenizing damage to the macroscale

The interface model, combined with the void-growth index, describes the development of damage between two grains of particular orientations embedded in a macroscale model. The multiscale damage model must homogenize this microscale damage and incorporate the effects of the macroscale damage on the macroscale structural response. Figure 4 describes the geometrical assumptions to link damage on the microscale with damage on the macroscale. These geometrical assumptions also ensure the model remains mesh-size independent, essentially by scaling the macroscale damage-to-failure based on the element size.

The process to calculate and incorporate damage has three parts, each performed at every load step, at each material point in a finite element model:

1. Calculate the crystal interface stresses, strains, and damage for n_{stacks} “stacks” of bicrystals, each with n_{per} bicrystals per stack. Generate microscale damage index values for each bicrystal.

2. A homogenization scheme converts the microscale damage index values at each bicrystal to one macroscale damage index for the material point.
3. Apply this macroscale damage on a plane in the finite element model.

The element size and grain size determine the number of grain stacks and number of bicrystals in a stack. l_n , l_s , and l_t are the lengths of the longest possible lines fitting inside an element in the **n**, **s**, and **t** directions. t_n , t_s , and t_t are the average grain sizes in the same directions. Then, based on simple geometric arguments:

$$n_{stacks} = \left(\frac{l_s}{t_s}\right) \left(\frac{l_t}{t_t}\right),$$

$$n_{per} = \frac{l_n}{2t_n}.$$

These numbers (rounded to the nearest integer) set the total number of crystals and bicrystal interfaces simulated at each material point – approximately equal to the number of pancake-shaped grains that fit inside the finite element containing the material point. This arrangement of grains also guides the homogenization to average microscale damage at each interface into macroscale damage at a material point. Recall that the previous section defined the damage at a bicrystal pair as the maximum value of damage in either crystal. Now we define the damage of a bicrystal stack as the maximum of the damage in each of the bicrystals in a stack. That is:

$$D_j = \max_{i=1}^{n_{per}} \{D_i\}.$$

Then define macroscale damage at a material point as:

$$D_{macro} = \sum_{j=1}^{n_{stacks}} D_j / n_{stacks} \quad (5)$$

That is, macroscale damage is the average damage in all the grain stacks at a material point. Since $D_j \in [0, 1]$ then $D \in [0, 1]$ and D is an appropriate damage index. This damage index implies a material point delaminates fully only when all of its grain stacks fail completely.

This approach for damage homogenization approximates the effect of delamination across a volume composed of pancake-shaped grains. Failure of a material point is taken as the inability to transmit load applied in an arbitrary direction. With this definition, a grain stack fails when the first grain boundary in the stack fails. Therefore, damage within a stack of grains is the maximum damage in all the bicrystals in the stack. Considering a collection of grain stacks tiled across a planar area, the collection of stacks fails only when all of the stacks fail – generating a complete failure path,

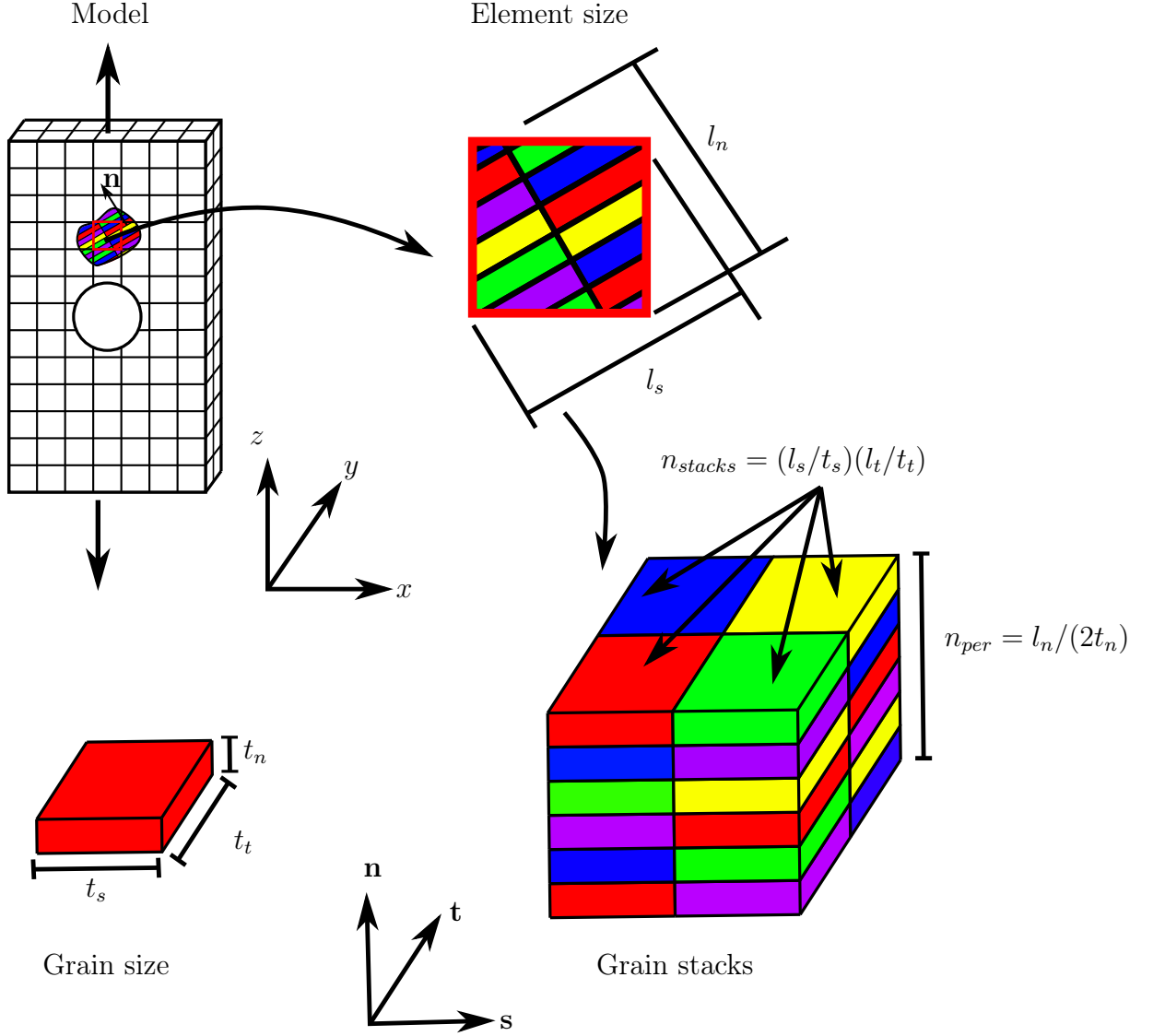


Fig. 4 Geometrical assumptions that provide the concept for the multi-scale homogenization technique upscaling microscale damage to macroscale material points.

representing a delamination crack, across the entire collection. The present model approximates this condition by taking the average of damage across the stacks. In the actual material (see Fig. 1), the failed grain boundaries are not in a single $s-t$ plane. Rather, the growing delamination crack jumps from one grain boundary to another, in a stair-step fashion. As a simplifying assumption, the present model neglects the energy required to propagate these stair-step jumps.

The damage homogenization technique retains approximate mesh-size independence. Arranging Eq. 5 at failure ($D_{macro} = 1$):

$$n_{stacks} = \sum_{j=1}^{n_{stacks}} D_j.$$

That is, the total damage accumulated across all grain stacks at failure increases as the number of grain stacks, and hence element size, increases. This reflects the geometry of the grain clusters – larger elements contain more grain stacks than smaller elements. Bažant and Lin [5] developed a similar technique to alleviate mesh-dependence of the smeared crack model for reinforced concrete – they scaled the fracture energy for the material with the element size.

Finally, the material point damage D on the macroscale does not represent isotropic failure of the material. Rather, the index represents damage localized to the $s-t$ plane, with normal vector \mathbf{n} . The model applies damage to the macroscale response through a projection matrix, which degrades the part of the stress tensor

lying on a plane with normal direction \mathbf{n} and transverse directions \mathbf{s} and \mathbf{t} . If $\boldsymbol{\sigma}^{ud}$ is the undamaged macroscale stress, the damaged stress is:

$$\boldsymbol{\sigma}^{macro} = (\mathbf{I}_{6 \times 6} - D\mathbf{P}_{6 \times 6}^D) \boldsymbol{\sigma}^{ud}$$

where the projection tensor $\mathbf{P}_{6 \times 6}^D$, described in the appendix, takes the projection of a stress tensor onto the plane with normal \mathbf{n} . A conventional finite element material model provides the undamaged macroscale constitutive response $\boldsymbol{\sigma}^{ud}$ – in this work, an isotropic von Mises plasticity model.

A few additional details remain. With the assumption that the failure plane evolves with the total material rotation \mathbf{R} , the unmodified damage projection correctly degrades stresses in the corotated intermediate configuration at large strains. As before, the large-strain, corotational stress update is identical to the small-strain stress update. Secondly, the new algorithmic tangent of the macroscale stress response, including damage, is:

$$\frac{\partial \mathbf{t}_{n+1}^{macro}}{\partial \Delta \mathbf{d}_{n+1}} = -\frac{\partial D_{n+1}}{\partial \Delta \mathbf{d}_{n+1}} \mathbf{P}_{6 \times 6}^D \mathbf{t}_{n+1}^{ud} + (\mathbf{I}_{6 \times 6} - D\mathbf{P}_{6 \times 6}^D) \mathbf{A}_{n+1}^{ud}$$

with \mathbf{A}_{n+1}^{ud} the algorithmic tangent of the undamaged macroscale stress update function – returned from the standard finite element material model. The term $\frac{\partial D_{n+1}}{\partial \Delta \mathbf{d}_{n+1}}$ changes depending on the particular choice of a damage index. To keep the damage index modular, the model makes one final assumption:

$$\mathbf{t}_{n+1}^{macro} = (\mathbf{I}_{6 \times 6} - D_n \mathbf{P}_{6 \times 6}^D) \mathbf{t}_{n+1}^{ud} \quad (6)$$

with the algorithmic tangent:

$$\mathbf{A}_{n+1}^{macro} = (\mathbf{I}_{6 \times 6} - D_n \mathbf{P}_{6 \times 6}^D) \mathbf{A}_{n+1}^{ud}. \quad (7)$$

That is, the integration becomes quasi-implicit: implicit for the stress update but explicit for the damage index. Notice the projection matrix $\mathbf{P}_{6 \times 6}^D$ is asymmetric – requiring an asymmetric assembly algorithm and an asymmetric linear solver to achieve quadratic convergence when solving the global finite element nonlinear force equations. Algorithm 2 describes the complete process.

The quasi-implicit integration procedure simplifies the stress update procedure. The model calculates the undamaged macroscale stress and algorithmic tangent using a standard finite element material model and adjusts the stress and tangent to reflect the damage index from the previous step using Eqs. 6 and 7. This decoupling limits the global step size. The damage index integration now lags the macroscale stress update, possibly requiring small load steps to achieve good accuracy. However, most simulations require small steps anyway to capture rapidly evolving damage at the grain boundaries.

2.4 Material parameters

Experimental data may be used to calibrate most of the model parameters. For example, macroscale standard tension and/or shear experiments enable fitting both the macroscale and microscale (crystal plasticity) stress response. Fracture toughness data aids in estimating the damage parameter α . Physical measurements provide the average grain thicknesses t_s , t_l , and t_t . The simulations in Section 4 provide an example using experimental data to calibrate the damage model. However, determining the crystallographic orientations of each grain represented at a material point is not straightforward. The grain orientations should represent the texture of the simulated material. Ideally, EBSD or similar measurements provide the actual orientations of the grains in the simulated region. However, this approach limits the predictive capabilities of the method.

A compromise retains a realistic texture but does not require *a priori* knowledge of the grain structure in a particular component. This option chooses grain orientations randomly from an orientation distribution function, or equivalently, from an experimentally measured texture. With this method, model results become non-deterministic – multiple simulations with the same properties yield different results for different, randomly selected, grain orientations at each material point. Conclusions drawn from the simulation results must reflect this variance.

3 Verification and model response

We implemented the damage model in WARP3D – an open-source, large deformation finite element software package (<https://code.google.com/p/warp3d/>). A previous work describes verification of the crystal plasticity formulation and algorithms to simulate the response of individual grains [38]. Von Mises plasticity provides the macroscale material model. However, any plasticity formulation could provide the macroscale response, including anisotropic models like Barlat et al. [4] and homogenized crystal plasticity. In addition to these material models, the damage formulation includes three further components: (1) the bicrystal interface model, (2) the damage index based on the Rice-Tracey parameter, and (3) the projection matrices to map macroscale damage index D onto a plane. The Rice-Tracey parameter approximately captures the physics of void-growth and the α parameter enables calibration of the damage model to experimental data (see next section); a specific verification of the damage index is not required. This section provides two simulations to verify the remaining aspects of the model.

Algorithm 2 Complete stress and damage update algorithm.

Input: $\Delta \varepsilon_{n+1}^{macro}$, macroscale stress state at t_n , macroscale damage at t_n , crystal states at time t_n , crystal damage at t_n .

1. Update crystal stresses, states to t_{n+1} with Algorithm 1.
2. Calculate crystal damage for each bicrystal pair with Eq. 4.
3. Calculate the macroscale damage at the next step, D_{n+1} , with the procedure in Section 2.3.
4. Calculate the undamaged macroscale stress, algorithmic tangent, and material history with a standard FE material model.
5. Calculate the damaged stress and tangent with Eqs. 6 and 7.

Return: σ_{n+1}^{macro} , \mathbf{A}_{n+1}^{macro} , D_{n+1} , updated crystal history and damage, updated macroscale material history.

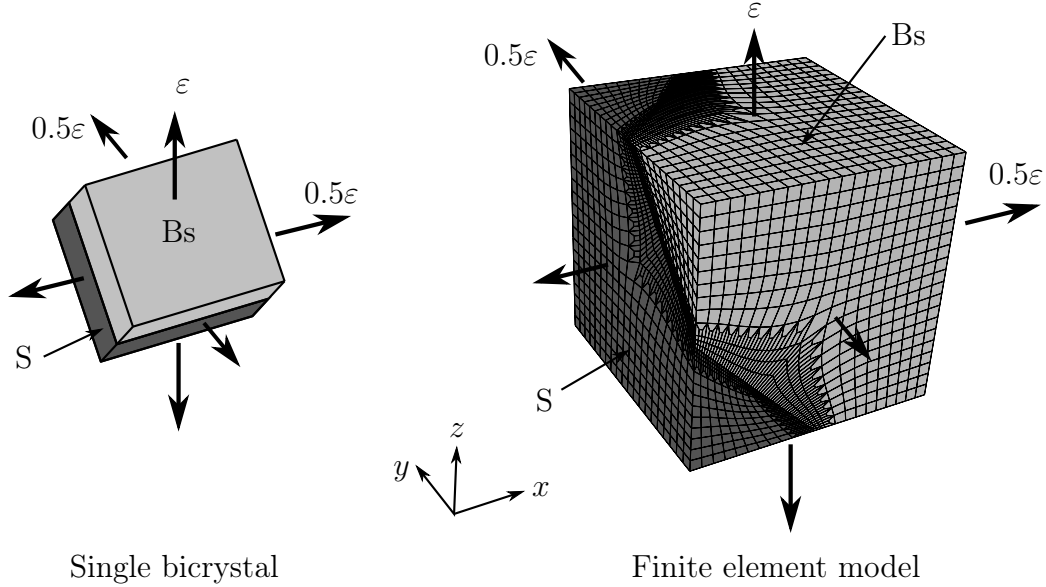


Fig. 5 Setup for the bicrystal verification analysis. Same displacement-controlled loading applied to both models.

3.1 Bicrystal interface response

Figure 5 shows the setup for verification of the bicrystal interface model. The verification compares the stresses at a grain boundary simulated with two different techniques: the compatibility/equilibrium interface model and a full finite element simulation. Both models represent a single bicrystal pair: a Bs (Bunge Euler angles $\phi_1 = 35^\circ$, $\Theta = 45^\circ$, $\phi_2 = 0^\circ$) / S ($\phi_1 = 59^\circ$, $\Theta = 29^\circ$, $\phi_2 = 63^\circ$) pair with interface normal $\mathbf{n} = [1 \ 1 \ 1] / \sqrt{3}$. The finite element simulation biases most of the mesh refinement to the grain boundary. The same loading is applied to each model in 100 equal load steps.

The reduced model generates a stress tensor for the Bs grain and a stress tensor for the S grain. The finite element simulation produces full stress fields over the grains. Figure 6 compares the mean stress (σ_m) calculated by the reduced model to the full field results of the finite element model. For this comparison, the FE results are from slices offset $h = 0.05$ mm from the grain boundary into the bulk of each grain – near enough to the boundary to include the effects of the ma-

terial interface. These plots show the relative difference $e_{\sigma_m} = |\sigma_m^{simple} - \sigma_m^{FE}(\mathbf{x})| / \sigma_m^{simple}$.

The results show low relative difference in both grains in the center of the model, away from the model surfaces. Similar results hold for the effective stress σ_e and the equivalent plastic strain $\bar{\varepsilon}^p$. At the edge of the model, boundary effects and the actual geometry of the modeled domain influence strongly the results. Away from boundary effects and near the interface plane, assumptions of the reduced model better represent the actual deformation of the material.

3.2 Planar damage projection

Figure 7 shows a single element model for testing the effects of macroscopic damage. Recall that the model projects macroscale damage index D anisotropically onto the plane of the grain boundary. For the model in Fig. 7, the damage plane has a normal in the y -direction. The damage parameter should affect the stress components forming the traction vector normal to the failure plane – σ_{yy} , σ_{xy} , and σ_{zy} – leaving the other compo-

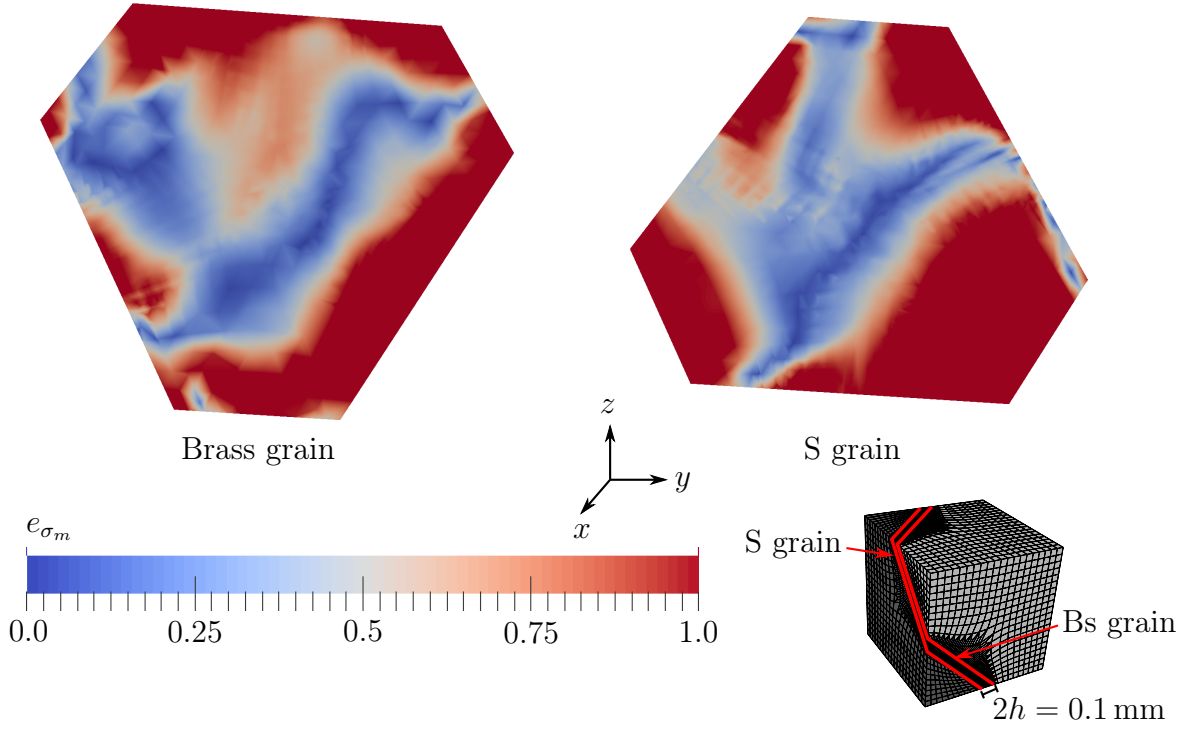


Fig. 6 Difference between the mean stress calculated with the simplified grain boundary model and mean stress results from a detailed finite element simulation of a bicrystal interface. Finite element results from planar slices $h = 0.05$ mm offset from the planar grain boundary into each grain. Difference is near zero at the center of the model, but increases near the model surface.

nents unaffected. This represents a delamination crack separating the material along the $x-z$ plane, eventually creating a free surface.

The test applies equal ε_{yy} normal strain and γ_{xy} shear strain to the element and imposes symmetry boundary conditions on element faces to prevent rigid body motion. The macroscale constitutive model is von Mises plasticity. Under this loading σ_{xx} , σ_{yy} , and σ_{xy} stresses develop – σ_{yy} and σ_{xy} from loading and σ_{xx} from constraint. The model projects damage onto the normal plane to reduce and eventually eliminate σ_{yy} and σ_{xy} as $D \rightarrow 1$.

Figure 7 shows the evolution of the three non-zero stress components with applied strain. The model works correctly – damage affects σ_{yy} and σ_{xy} but does not affect σ_{xx} . Similar tests confirm the model correctly projects damage onto other planes – including planes with normals not parallel to the model coordinate system.

4 Application to 2195 Al-Li

This section applies the damage model to represent delamination fracture in 2195 Al-Li. Tables 1 and 2 summarize tensile and fracture test data from the open lit-

erature. The texture and grain structure of the material cause both the tensile and fracture properties to depend on orientation. In particular, splitter configuration (TL and SL in Fig. 2) specimens have a much lower effective toughness than divider and arrestor configurations.

Application of the damage model to 2195 Al-Li requires calibration of several components:

1. Determine the texture of the material to select grain orientations for the bicrystal model. This work samples orientations randomly from an experimentally measured textures in a plate sample of 2195 [51].
2. Determine the average grain size of the material – here using the same EBSD dataset.
3. Fit a finite element material model to the macroscale response of the material – here fit the tension test data in Table 1 to an isotropic von Mises model.
4. Fit the microscale crystal plasticity model to the microscale (undamaged) material response – this work fits a Taylor homogenized polycrystal of 500 orientations drawn randomly from the EBSD dataset to the macroscale tension test data.
5. Determine the damage index parameter α by comparing a small-scale-yielding fracture model of a splitter configuration to experimental fracture toughness data from splitter configuration tests.

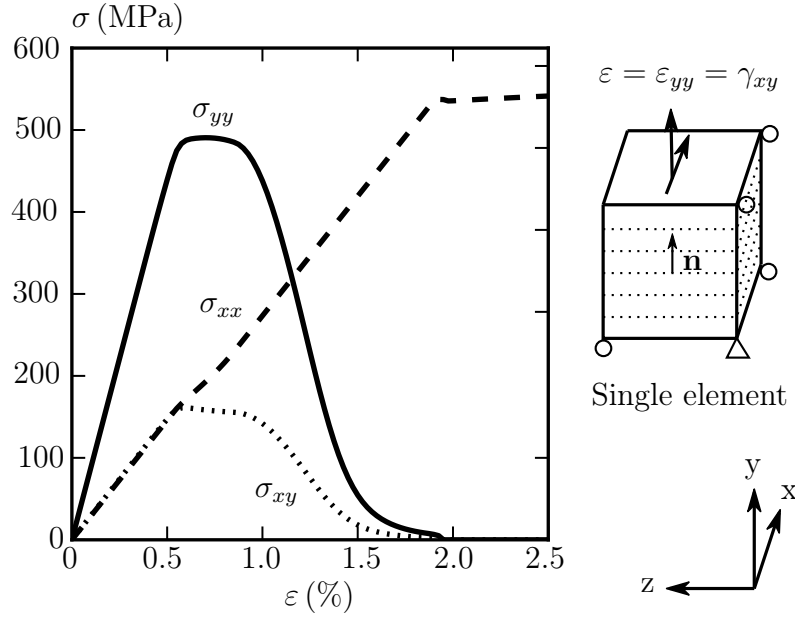


Fig. 7 Single element example demonstrating the macroscale planar damage projection. The single element is loaded with displacements to enforce equal strains in the yy normal and xy shear directions and symmetry on three faces to constrain the model. The interface/failure plane has a normal vector in the y -direction – parallel to the applied loading. When the element completely fails ($D = 1.0$ at all Gauss points) the normal stress σ_{yy} and shear stress σ_{xy} fall to zero, but the transverse normal stress σ_{xx} remains unaffected.

Configuration	σ_Y (MPa)	σ_U (MPa)	%EL	Source
L	574.3	609.5	8.5	[30]
T	550.9	588.8	11.2	"
L	574.3	615.7	10.5	[2]
T	542.6	586.1	10.0	"
45° L-T	506.7	553.6	12.3	"
L	510.23, 524.7, 544.0	573.0, 575.0, 586.1	7.0, 8.0, 6.5	[8]
"	533.7, 514.4, 537.1	582.6, 568.1, 581.2	6.5, 7.8, 8.3	"

Table 1 Uniaxial tension test data for 2195 Al-Li, from a variety of sources in different configurations. Here σ_Y is the room temperature yield stress, σ_U is the ultimate tensile strength, and %EL is the percent elongation at failure.

Specimen type	Configuration	K_{Ic} (MPa \sqrt{m})	Source
C(T)	LS	47.5	[29]
	SL	30.2, 32.9	"
	LT	49.7	"
M(T)	LS	73.71, 70.9, 73.1, 74.9	"
Unknown	Splitter	29.6, 25.4, 34.9	[7]
Unknown	TL	25.4, 34.9	[8]

Table 2 Room temperature fracture toughness data for 2195 Al-Li in a variety of configurations.

4.1 Fitting of model parameters

The data summarized in Tables 1 and 2 and an experimentally measured orientation for 2195 Al-Li form the basis for the model calibration. The macroscale von Mises plasticity model matches the uniaxial tension test data summarized in Table 1. The strong texture of rolled Al-Li causes the tension test data to vary with material orientation. The parameters for the von Mises

model represent a fit to an average of the data from all different orientations. Figure 8 shows the fit to the data and Table 3 summarizes the macroscopic material model parameters.

The CP model represents the microconstitutive response of individual grains. Here the model evolves slip system hardening with a Voce law following the formulation described in Messner et al. [38]. The CP model parameters match the response of a homogenized poly-

Parameter	Description	Value
E	Young's modulus	78800 MPa
ν	Poisson's ratio	0.33
σ_Y	Yield stress	517 MPa
n_{power}	Power law hardening coefficient	18.5

Table 3 Material parameters for macroscale von Mises material model.

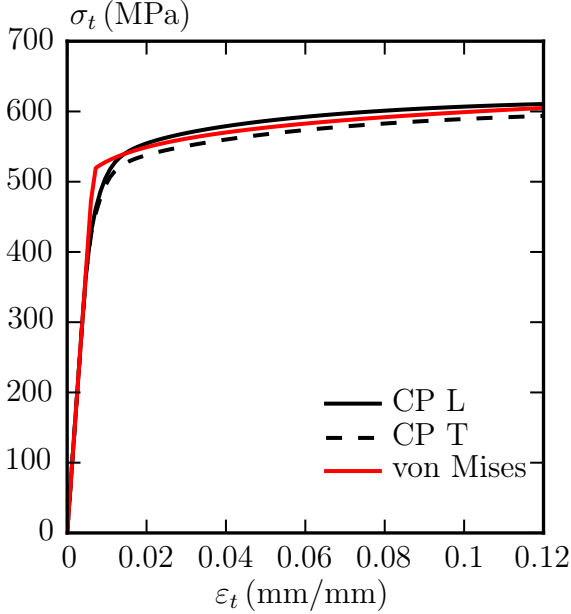


Fig. 8 The fit of the macroscopic von Mises material model and the homogenized microscale crystal plasticity material model, both in uniaxial tension loading. The crystal plasticity model captures the effect of material orientation.

crystal representing 500 random orientations, drawn from the 2195 texture, to the macroscale uniaxial tension test data. The homogenized crystal plasticity model captures the effect of material orientation on the uniaxial stress/strain response. Elastic parameters are isotropic elastic. See Fig. 8 for a comparison to the macroscale von Mises model and Table 4 for the material parameters.

The small scale yielding (SSY) fracture model shown in Fig. 9 is adopted to calibrate the microscale damage index constant α . The SSY model represents a long primary crack loaded with the Mode I asymptotic crack front displacements [1]. Small scale yielding conditions apply: at $K_{Ic} \approx 45 \text{ MPa}\sqrt{\text{m}}$ the plastic zone radius extends to about 1 mm from the crack front – much less than the in-plane dimensions of a typical test specimen or manufactured component. Material near the primary crack front and in the plastic zone undergoes damage as described above. Outside this region, undamaged von Mises plasticity represents the material response. The thickness of the model ($B/2 = 5 \text{ mm}$) approximates the thickness of the C(T) specimen test from Hernquist [29].

Symmetry reduces the modeled region by one-fourth: in the y - and z -directions.

The SSY model can represent any delamination configuration (see Fig. 2) by changing the vectors \mathbf{n} , \mathbf{s} , and \mathbf{t} defining the grain coordinate system. For example, when $\mathbf{n} = [0 \ 1 \ 0]$ (\mathbf{s} and \mathbf{t} arbitrary unit vectors orthogonal to \mathbf{n} and each other) the model represents a crack splitter configuration. In addition to aligning failure/grain boundary plane, the model must also rotate the Euler angles representing the texture of the material into the new coordinate system. Experiments suggest delamination in the splitter configuration should supplant transgranular cracking and propagate an approximately straight primary crack. Figure 10 shows the damage model correctly reproduces this behavior – as the load on the model (K_I^{app}) increases, damage develops ahead of the primary crack front on the primary crack plane. When the damage parameter in an element reaches $D = 1$ that element completely releases the traction components in the y -direction – thereby advancing the primary crack front.

Calibration of the damage parameter α requires the value of α such that primary crack advance in the model occurs at $K_I^{app} = K_{Ic}^{split}$, where K_{Ic}^{split} is the average of the initiation toughness values in Table 2 for SL and ST configurations. That is, adjust α until the first row of elements ahead of the primary crack fails at $K_I^{app} = 30.5 \text{ MPa}\sqrt{\text{m}}$. The result of this calibration is $\alpha = 0.25$.

4.2 Delamination crack growth

Figure 10 shows the damage index D and the corresponding mean stress field for three different configurations: an LS arrestor configuration, a TL divider configuration, and a SL splitter configuration. Deep red values indicate element failure ($D = 1.0$), blue values represent undamaged elements. The FE model is identical for all three simulations – only the specified directions of \mathbf{n} , \mathbf{s} , and \mathbf{t} vectors and the rotations describing the material texture in the global coordinates change for each different fracture configuration. For comparison, the figure also shows the mean stress field for an undamaged von Mises material.

Delamination crack growth patterns shown in Fig. 10 differ for each of the three configurations and match experimental observations. The following discussion describes the delaminations that develop in each of the three configurations and links the type of delamination growth to its effect on the macroscale stress and strain fields.

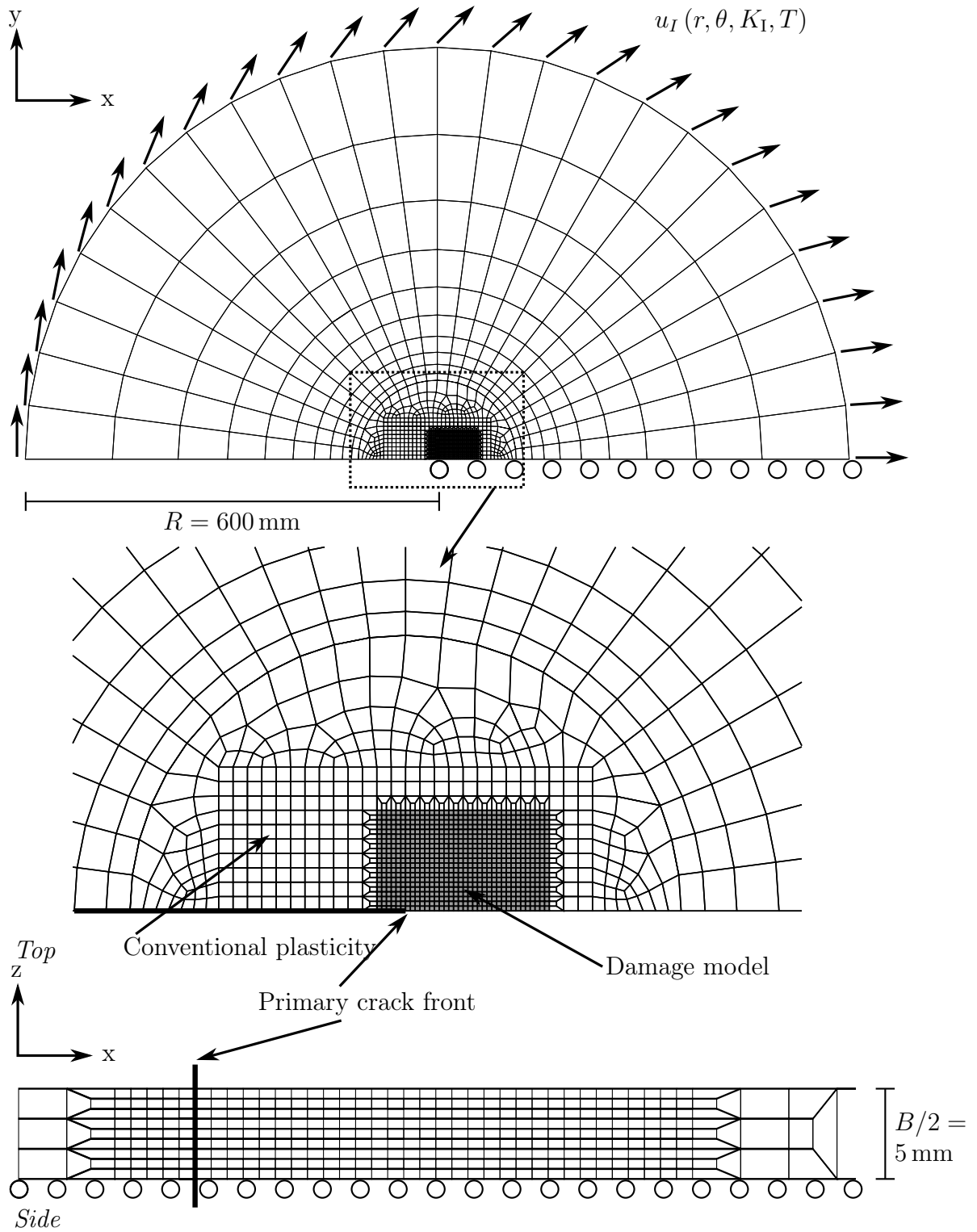


Fig. 9 This SSY model supports calibration of the damage model parameter α using experimental fracture test data and simulation of delamination crack growth for three material configurations. Here $R = 600$ mm and $B/2 = 5$ mm – matching the C(T) specimen thickness from [29]. The damage model developed in this work represents the region of material near the primary crack. Outside this region, an undamaged von Mises plasticity model represents the response.

Parameter	Description	Value
E	Young's modulus	78800 MPa
ν	Poisson's ratio	0.33
n	Rate sensitivity coefficient	20
θ_0	Initial slip system hardening slope	150 MPa
τ_y	Intrinsic slip system strength	190 MPa
τ_v	Maximum amount of slip system hardening	25 MPa
m	Voce law power coefficient	1
α	Rice-Tracy damage model parameter	0.25

Table 4 Material parameters and values for the microscale crystal plasticity model and the calibrated microscale damage index coefficient α .

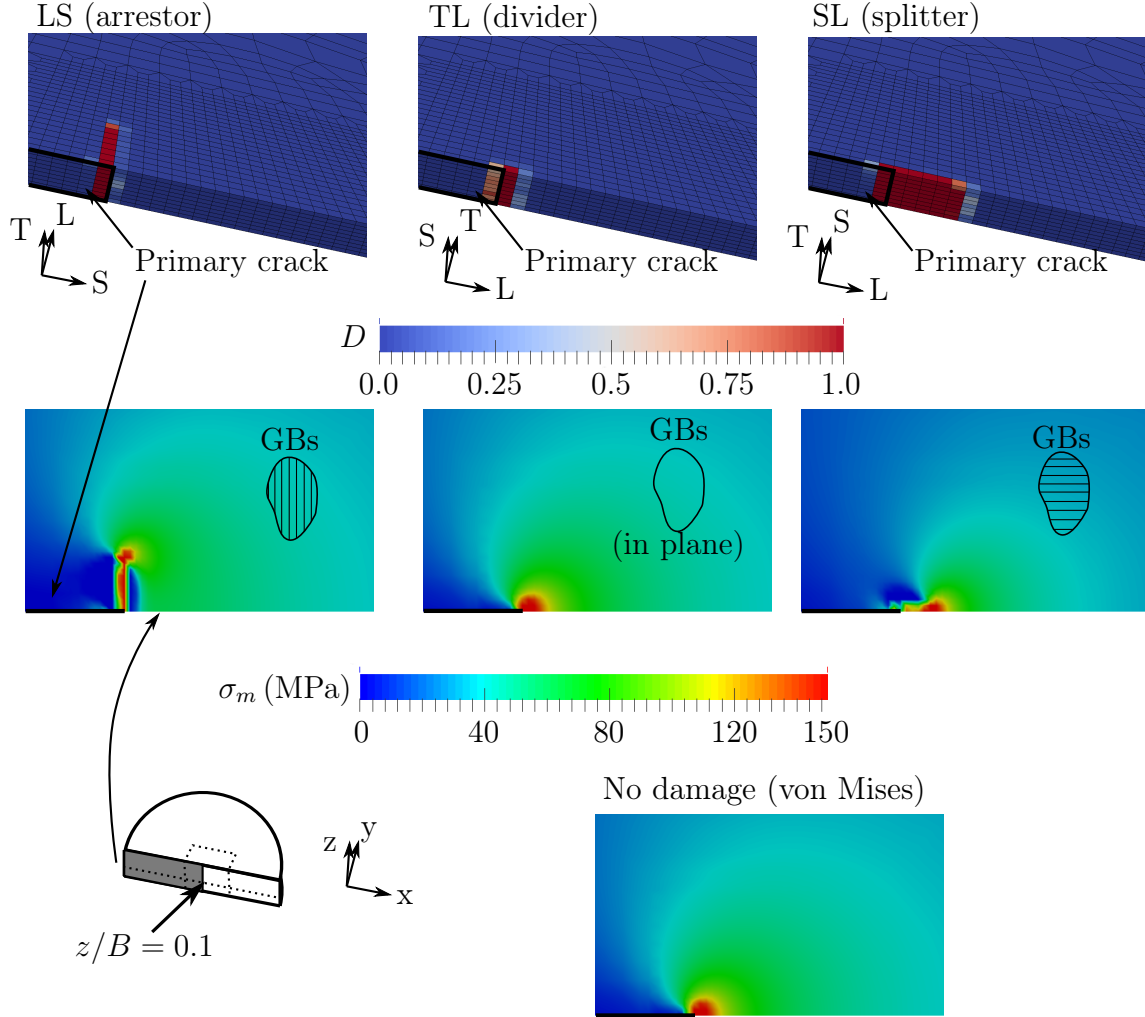


Fig. 10 Amount and direction of delamination crack growth in three standard configurations and the resulting mean stress fields. Simulations use the calibrated material properties ($\alpha = 0.25$) and have the same loading ($K_I = 60.0 \text{ MPa}\sqrt{\text{m}}$). For each configuration, the top image shows the value of the damage parameter D , with dark red values indicating complete delamination failure. The lower row of images shows the mean stress fields on a planar slice through the thickness of the model, near the symmetry plane ($z/B = 0.1$). The lowest image shows the mean stress field for an undamaged model.

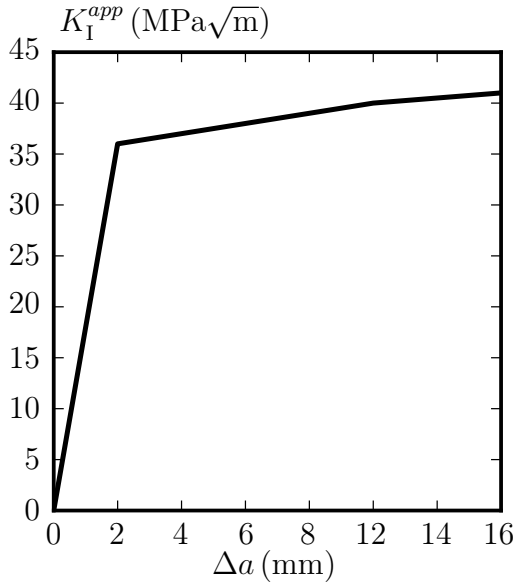


Fig. 11 A K - Δa plot showing the crack extension of the *arrestor* delamination versus the applied Mode I stress intensity factor.

Arrestor

In the arrestor configuration a comparatively long delamination (greater than 10 grain widths/100 grain thicknesses) develops perpendicular to the primary crack front. Such a perpendicular delamination matches the crack growth pattern observed in arrestor M(T) tests by Hernquist [29]. The arrestor delamination propagates under the substantial σ_{xx} stress concentration that develops near the primary crack front.

Figure 11 plots the extension of the arrestor delamination versus the applied Mode I loading. The arrestor crack begins to extend well before the primary crack would advance – Table 2 shows primary crack growth in arrestor configurations requires at least $K_I \approx 45 \text{ MPa}\sqrt{\text{m}}$ whereas the figure shows arrestor delamination growth occurring at $K_I \approx 35 \text{ MPa}\sqrt{\text{m}}$.

The arrestor crack relieves the mean stress concentration near the initial primary crack front but generates a region of increased mean stress near the new, additional front at the tip of the delamination. Previous simulations and experiments also exhibit this stress rearrangement, reducing the driving stress near the initial, primary crack front while increasing the stress near the delamination front. In addition, mean stress in the model remains elevated along the length of the arrestor crack, behind the initial primary crack front. These correspond to mean residual stresses expected from crack advance – only here crack advance occurs perpendicular to the initial primary crack.

Splitter

In the splitter configuration damage develops ahead of the primary crack along the initial crack plane. This is also the crack growth pattern observed in experiments. The Mode I field of the primary crack drives the splitter delamination, essentially advancing the primary, transgranular crack.

The growing splitter delamination generates a mean stress field corresponding to the stresses expected from straight primary crack growth – the stress concentration advances with the growth of the crack, leaving behind residual stresses in the wake of the crack front.

Divider

In the divider configuration, damage remains localized near the primary crack front and near the primary crack plane. Post-failure observations of divider configuration fracture tests typically show longer divider delaminations segmenting the primary crack plane [2]. The lack of a growth mechanism for primary, transgranular cracks in the simulation explains this discrepancy. Divider cracking generally occurs simultaneously with transgranular crack advance. Divider cracks do not halt or turn the primary crack (like arrestor configurations) or supplant transgranular cracking (like splitter configurations). With an advancing primary crack, damage at the crack front distributes across the crack plane, thereby generating a delamination growth pattern similar to the experimental observations.

The results imply that in thin plate specimens macroscale forces do not drive a divider microcrack. In a thin plate the magnitude of the through-thickness σ_{zz} stress remains much smaller than the in-plane σ_{xx} and σ_{yy} stresses that drive arrestor and splitter cracks. However, in thicker specimens elevated through-thickness stresses develop as a consequence of stress triaxiality. Here the macroscale stress field may propagate a divider delamination with or without accompanying growth of the primary crack.

In the divider configuration, the stresses do not change significantly from the undamaged model. Since damage remains isolated very near the primary crack front it does not significantly affect the material away from the crack. Near the primary crack front damage in the divider configuration lowers the mean stress as the damage projected on the xy plane lowers the σ_{zz} normal stress component.

The effect of delamination on measured macroscopic toughness

The reduction in mean stress observed in the arrestor and, to a lesser extent, divider configurations readily explains why these geometries have a higher measured toughness than the splitter configuration. The damage caused by delaminations reduces the stresses near the primary crack, lowering the driving force for primary crack extension. This result, obtained here with the multiscale damage model in a macroscale simulation, agrees with our previous simulations on the microscale with crystal plasticity models for small groups of grains [37, 39].

The influence of texture on delamination cracking

Figure 10 shows results for a single simulation in each of the three configurations. Recall that the model selects the crystal orientations of the bicrystal pairs represented at each material point randomly from an experimentally measured texture. The particular selection of orientations, especially near the primary crack front, affects the predicted extension of delamination cracks. Figure 12 shows one example of this variability. The macroscale damage index is shown for three simulations of splitter configurations at the same far field loading ($K_I = 32 \text{ MPa}\sqrt{\text{m}}$) – essentially showing the amount of splitter delamination advance along the primary crack plane. Each simulation predicts a different amount of crack growth – ranging from 6 to 10 mm. Fracture tests on 2195 Al-Li also show this variability – geometrically identical specimens from the same plate of material exhibit different amounts of delamination crack growth depending on the grain orientations near the primary crack front. The interpretation of simulations representing delamination with the multiscale damage model developed in this work must take into account this variation.

5 Conclusions

This work develops a multiscale model of intergranular damage and applies the model to delamination cracking in 2195 Al-Li. The damage model represents the key mechanics of failure over grain boundaries – the mesoscale deformation of crystalline grains, the compatibility/equilibrium requirements on grain boundaries, and the mesoscale mechanism of intergranular damage. A mesh-size independent homogenization procedure maps damage over grain boundaries at the microscale to damage on the macroscale. Projection tensors apply the

macroscale damage index to a plane in the finite element model – an approach which essentially extends the smeared crack model to nonlinear, large deformation materials. Example simulations verify the bicrystal interface model and the damage projection matrices.

When applied to 2195 Al-Li, the damage model reproduces key features of experimentally observed delamination cracking:

- Delamination crack growth varies with material orientation – matching the behavior of experiments on standard arrestor, divider, and splitter configurations
- In the arrestor and divider configurations, delamination cracking, represented by the multiscale damage model, shields the primary crack by reducing the stresses near the crack front. In the arrestor configuration, delamination effectively turns the primary crack 90° – behavior observed in M(T) fracture tests.
- By selecting orientations of the bicrystal pairs randomly from an experimentally measured dataset, the damage model reproduces the strong effect of material texture on delamination crack growth.

The damage model can represent intergranular failure in other materials with a similar pancake-shaped grain structure through calibration of the macroscale and microscale constitutive models and by selecting an intergranular damage index to account for the mechanism of microscale damage. With different geometric assumptions the model could also apply to materials with a more complex grain geometry. For materials with hexagonal grains, the model might track and homogenize damage on six planes, instead of the single plane considered for delamination in Al-Li. Such a model would then define damage to the macroscale stress/strain response with a multiplicative composition of the projection tensors described in Eqs. 6 and 7:

$$\sigma_{macro} = \left\{ \prod_{i=1}^6 \left(\mathbf{I}_{6 \times 6} - D^{(i)} \mathbf{P}_{6 \times 6}^{D, (i)} \right) \right\} \sigma^{ud}$$

where $D^{(i)}$ is the damage index and $\mathbf{P}_{6 \times 6}^{D, (i)}$ the projection matrix for each of the six faces of the hexagonal grains.

Acknowledgements

M. C. Messner's contribution was in part supported by the Department of Defense (DoD) through the National Defense Science & Engineering Graduate Fellowship (NDSEG) Program and in part performed under the auspices of the U.S. Department of Energy by

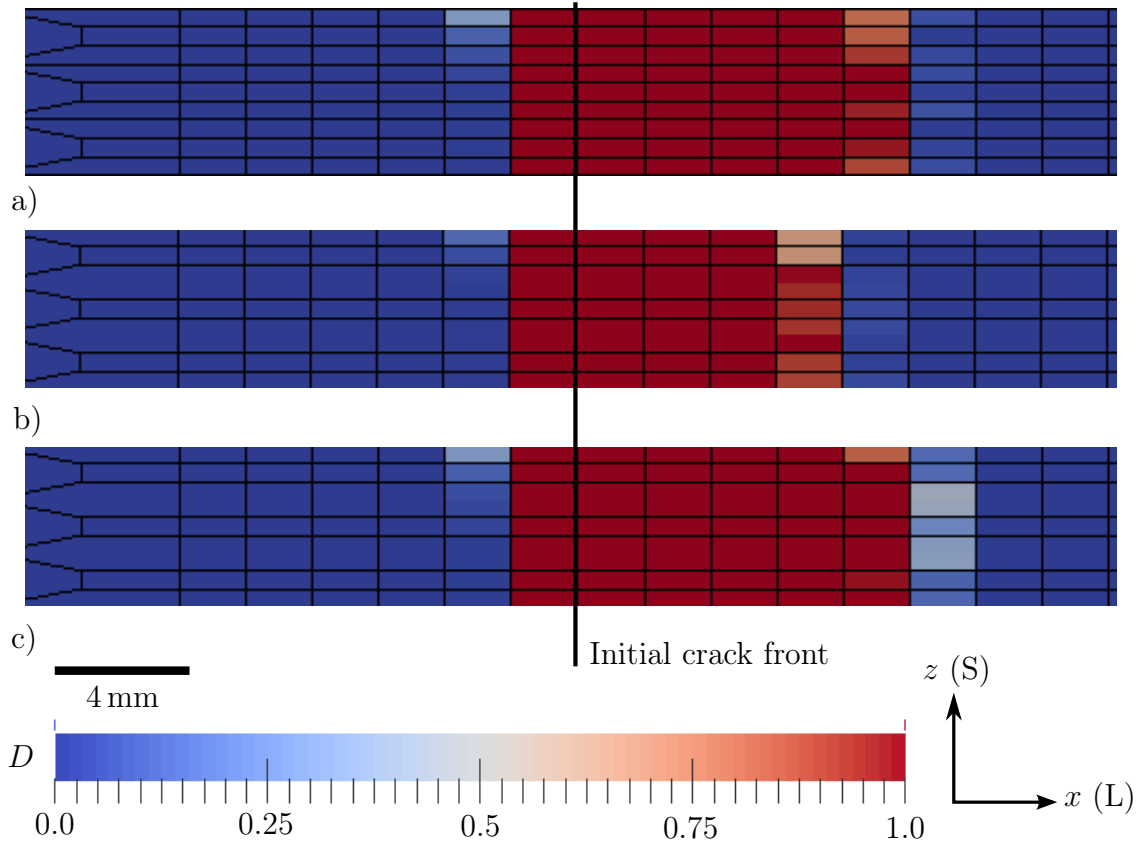


Fig. 12 Three simulations in the SL splitter configuration, all with the same loading ($K_I = 32 \text{ MPa}\sqrt{\text{m}}$) and same material properties, but different grain orientations at each material point – chosen randomly from an experimentally measured texture. This figure shows the variability inherent in this method of selecting grain orientations. Each simulation develops different amounts of splitter delamination crack growth and correspondingly different stress/strain fields.

Lawrence Livermore National Laboratory under Contract DE-AC52-07NA27344 (LLNL-JRNL-666218). A. J. Beaudoin recieved support through the U.S. Department of Energy under Contract DEFG36-05GO15049. R. H. Dodds received support from the M. T. Geoffrey Yeh Chair Fund.

A Projection matrices

This appendix lists the components of the three projection tensors describe above – $\mathbf{P}_{3 \times 6}^e$, $\mathbf{P}_{3 \times 6}^c$, and $\mathbf{P}_{6 \times 6}^D$. Each matrix is a combination of the components of the orthogonal coordinate system describing the interface plane/grain boundaries with normal vector \mathbf{n} and transverse vectors \mathbf{s} and \mathbf{t} . Let the components of these vectors be:

$$\mathbf{n} = [n_1 \ n_2 \ n_3]^T$$

$$\mathbf{s} = [s_1 \ s_2 \ s_3]^T$$

$$\mathbf{t} = [t_1 \ t_2 \ t_3]^T$$

As described above, under large deformations and rotations these vectors remain constant in the corotational configuration. The form of the projection matrices depends on the Voigt notation

used in the finite element framework. The particular Voigt notation in this work is:

$$\boldsymbol{\epsilon} \rightarrow [\epsilon_{11} \ \epsilon_{22} \ \epsilon_{33} \ 2\epsilon_{12} \ 2\epsilon_{23} \ 2\epsilon_{13}]^T$$

$$\boldsymbol{\sigma} \rightarrow [\sigma_{11} \ \sigma_{22} \ \sigma_{33} \ \sigma_{12} \ \sigma_{23} \ \sigma_{13}]^T.$$

The components of each projection are:

$$\mathbf{P}_{3 \times 6}^e = \begin{bmatrix} n_1 & 0 & 0 & n_2 & 0 & n_3 \\ 0 & n_2 & 0 & n_1 & n_3 & 0 \\ 0 & 0 & n_3 & 0 & n_2 & n_1 \end{bmatrix}$$

$$\mathbf{P}_{3 \times 6}^c =$$

$$\begin{bmatrix} s_1^2 & s_2^2 & s_3^2 & s_1 s_2 & s_2 s_3 & s_1 s_3 \\ t_1^2 & t_2^2 & t_3^2 & t_1 t_2 & t_2 t_3 & t_1 t_3 \\ s_1 t_1 & s_2 t_2 & s_3 t_3 & \frac{1}{2}(s_2 t_1 + s_1 t_2) & \frac{1}{2}(s_2 t_3 + s_3 t_2) & \frac{1}{2}(s_3 t_1 + s_1 t_3) \end{bmatrix}$$

and

$$\mathbf{P}_{6 \times 6}^D = \begin{bmatrix} p_{11} & p_{12} & p_{13} & p_{14} & p_{15} & p_{16} \\ p_{21} & p_{22} & p_{23} & p_{24} & p_{25} & p_{26} \\ p_{31} & p_{32} & p_{33} & p_{34} & p_{35} & p_{36} \\ p_{41} & p_{42} & p_{43} & p_{44} & p_{45} & p_{46} \\ p_{51} & p_{52} & p_{53} & p_{54} & p_{55} & p_{56} \\ p_{61} & p_{62} & p_{63} & p_{64} & p_{65} & p_{66} \end{bmatrix}$$

with:

$$\begin{aligned}
p_{11} &= n_1^2 (n_1^2 + 2 (s_1^2 + t_1^2)) \\
p_{12} &= n_1 n_2 (n_1 n_2 + 2 s_1 s_2 + 2 t_1 t_2) \\
p_{13} &= n_1 n_3 (n_1 n_3 + 2 s_1 s_3 + 2 t_1 t_3) \\
p_{14} &= 2 n_1 (n_1 (s_1 s_2 + t_1 t_2) + n_2 (s_1^2 + t_1^2) + n_2 n_1^2) \\
p_{15} &= 2 n_1 (n_3 (s_1 s_2 + t_1 t_2) + n_2 (s_1 s_3 + t_1 t_3) + n_1 n_2 n_3) \\
p_{16} &= 2 n_1 (n_1 (s_1 s_3 + t_1 t_3) + n_3 (s_1^2 + t_1^2) + n_3 n_1^2) \\
p_{21} &= n_1 n_2 (n_1 n_2 + 2 s_1 s_2 + 2 t_1 t_2) \\
p_{22} &= n_2 (2 n_2 (s_2^2 + t_2^2) + n_2^3) \\
p_{23} &= n_2 n_3 (n_2 n_3 + 2 s_2 s_3 + 2 t_2 t_3) \\
p_{24} &= 2 n_2 (n_2 (s_1 s_2 + t_1 t_2) + n_1 (n_2^2 + s_2^2 + t_2^2)) \\
p_{25} &= 2 n_2 (n_2 (s_2 s_3 + t_2 t_3) + n_3 (s_2^2 + t_2^2) + n_3 n_2^2) \\
p_{26} &= 2 n_2 (n_3 (s_1 s_2 + t_1 t_2) + n_1 (n_2 n_3 + s_2 s_3 + t_2 t_3)) \\
p_{31} &= n_1 n_3 (n_1 n_3 + 2 s_1 s_3 + 2 t_1 t_3) \\
p_{32} &= n_2 n_3 (n_2 n_3 + 2 s_2 s_3 + 2 t_2 t_3) \\
p_{33} &= n_3^2 (n_3^2 + 2 (s_3^2 + t_3^2)) \\
p_{34} &= 2 n_3 (n_2 (s_1 s_3 + t_1 t_3) + n_1 (n_2 n_3 + s_2 s_3 + t_2 t_3)) \\
p_{35} &= n_3 (2 n_3 (s_2 s_3 + t_2 t_3) + 2 n_2 (n_3^2 + s_3^2 + t_3^2)) \\
p_{36} &= n_3 (2 n_3 (s_1 s_3 + t_1 t_3) + 2 n_1 (n_3^2 + s_3^2 + t_3^2)) \\
p_{41} &= n_1 (n_1 (s_1 s_2 + t_1 t_2) + n_2 (s_1^2 + t_1^2) + n_2 n_1^2) \\
p_{42} &= n_2 (n_2 (s_1 s_2 + t_1 t_2) + n_1 (n_2^2 + s_2^2 + t_2^2)) \\
p_{43} &= n_3 (n_2 (s_1 s_3 + t_1 t_3) + n_1 (n_2 n_3 + s_2 s_3 + t_2 t_3)) \\
p_{44} &= n_1^2 (2 n_2^2 + s_2^2 + t_2^2) + 2 n_2 n_1 (s_1 s_2 + t_1 t_2) + n_2^2 (s_1^2 + t_1^2) \\
p_{45} &= n_2 (n_3 (s_1 s_2 + t_1 t_2) + n_2 (s_1 s_3 + t_1 t_3)) + \\
&\quad n_1 (n_2 (s_2 s_3 + t_2 t_3) + n_3 (s_2^2 + t_2^2) + 2 n_3 n_2^2) \\
p_{46} &= n_1^2 (2 n_2 n_3 + s_2 s_3 + t_2 t_3) + \\
&\quad n_1 (n_3 (s_1 s_2 + t_1 t_2) + n_2 (s_1 s_3 + t_1 t_3)) \\
&\quad + n_2 n_3 (s_1^2 + t_1^2) \\
p_{51} &= n_1 (n_3 (s_1 s_2 + t_1 t_2) + n_2 (s_1 s_3 + t_1 t_3) + n_1 n_2 n_3) \\
p_{52} &= n_2 (n_2 (s_2 s_3 + t_2 t_3) + n_3 (s_2^2 + t_2^2) + n_3 n_2^2) \\
p_{53} &= n_3 (n_3 (s_2 s_3 + t_2 t_3) + n_2 (n_3^2 + s_3^2 + t_3^2)) \\
p_{54} &= n_2 (n_3 (s_1 s_2 + t_1 t_2) + n_2 (s_1 s_3 + t_1 t_3)) + \\
&\quad n_1 (n_2 (s_2 s_3 + t_2 t_3) + n_3 (s_2^2 + t_2^2) + 2 n_3 n_2^2) \\
p_{55} &= n_2^2 (2 n_3^2 + s_3^2 + t_3^2) + 2 n_3 n_2 (s_2 s_3 + t_2 t_3) + n_3^2 (s_2^2 + t_2^2) \\
p_{56} &= n_3 (n_3 (s_1 s_2 + t_1 t_2) + n_2 (s_1 s_3 + t_1 t_3)) + \\
&\quad n_1 (n_3 (s_2 s_3 + t_2 t_3) + n_2 (2 n_3^2 + s_3^2 + t_3^2)) \\
p_{61} &= n_1 (n_1 (s_1 s_3 + t_1 t_3) + n_3 (s_1^2 + t_1^2) + n_3 n_1^2) \\
p_{62} &= n_2 (n_3 (s_1 s_2 + t_1 t_2) + n_1 (n_2 n_3 + s_2 s_3 + t_2 t_3)) \\
p_{63} &= n_3 (n_3 (s_1 s_3 + t_1 t_3) + n_1 (n_3^2 + s_3^2 + t_3^2)) \\
p_{64} &= n_1^2 (2 n_2 n_3 + s_2 s_3 + t_2 t_3) + \\
&\quad n_1 (n_3 (s_1 s_2 + t_1 t_2) + n_2 (s_1 s_3 + t_1 t_3)) + n_2 n_3 (s_1^2 + t_1^2) \\
p_{65} &= n_3 (n_3 (s_1 s_2 + t_1 t_2) + n_2 (s_1 s_3 + t_1 t_3)) + \\
&\quad n_1 (n_3 (s_2 s_3 + t_2 t_3) + n_2 (2 n_3^2 + s_3^2 + t_3^2)) \\
p_{66} &= n_1^2 (2 n_3^2 + s_3^2 + t_3^2) + 2 n_3 n_1 (s_1 s_3 + t_1 t_3) + n_3^2 (s_1^2 + t_1^2).
\end{aligned}$$

References

1. T. L. Anderson. *Engineering fracture mechanics*. Taylor & Francis Group, 2005.
2. H. W. Babel, B. Farahmand, and A. Yousefiani. Assessment of delaminations in current Aluminum-Lithium alloys. Technical report, Boeing, 2003.
3. S. K. Banerji, C. J. McMahon, Jr., and H. C. Feng. Intergranular fracture in 4340-type steels: effects of impurities and hydrogen. *Metallurgical Transactions*, 1987.
4. F. Barlat, H. Aretz, J. W. Yoon, M. E. Karabin, J. C. Brem, and R. E. Dick. Linear transformation-based anisotropic yield functions. *International Journal of Plasticity*, 21:1009–1039, 2005.
5. Z. P. Bažant and F. Lin. Nonlocal smeared cracking model for concrete fracture. *Journal of Structural Engineering*, 114 (11):2493–2510, 1988.
6. A. J. Beaudoin, M. Obstalecki, W. Tayon, M. Hernquist, R. Mudrock, P. Kenesei, and U. Lienert. In situ assessment of lattice strain in an Al-Li alloy. *Acta Materialia*, In press, 2013.
7. P. S. Chen and W. P. Stanton. A new aging treatment for improving cryogenic toughness of the main structural alloy of the super lightweight tank. Technical Report 108524, NASA, 1996.
8. P. S. Chen and W. P. Stanton. Cryogenic fracture toughness imprprove for the super-lightweight tank's main structural alloy. Technical Report 2002-21547, NASA, 2002.
9. A. C. F. Cocks and M. F. Ashby. Intergranular fracture during power-law creep under multiaxial stresses. *Metal Science*, pages 395–402, 1980.
10. R. Crooks, M. S. Domack, and J. A. Wagner. Microtexture and nanoindentation study of delamination cracking in Al-Cu-Li-X alloys. *WIT Transactions on the Built Environment*, 85:549–557, 2006.
11. P.S. De, R. S. Mishra, and J. A. Baumann. Characterization of high cycle fatigue behavior of a new generation aluminum lithium alloy. *Acta Materialia*, 59:5946–5960, 2011.
12. Y. d'Escata and J. C. Devaux. Numerical study of the initiation, stable crack growth, and maximum load with a ductile fracture criterion based on the growth of holes. In *ASTM STP 668*, pages 229–248. American Society of Testing and Materials, 1979.
13. G. H. Edward and M. F. Ashby. Intergranular fracture during power-law creep. *Acta Metallurgica*, 27:1505–1518, 1979.
14. L. P. Evers, D. M. Parks, W. A. M. Brekelmans, and M. G. D. Geers. Crystal plasticity model with enhanced hardening by geometrically necessary dislocation accumulation. *Journal of the Mechanics and Physics of Solids*, 50:2403–2424, 2002.
15. D. Farkas, H. Van Swygenhoven, and P. M. Derlet. Intergranular fracture in nanocrystalline metals. *Physical Review B*, 66, 2002.
16. J. Fish and V. Belsky. Multigrid method for periodic heterogeneous media Part 1: Convergence studies for one-dimensional case. *Computer Methods in Applied Mechanics and Engineering*, 126:1–16, 1995.
17. J. Fish and V. Belsky. Multi-grid method for periodic heterogeneous media Part 2: Multiscale modeling and quality control in multidimensional case. *Computer Methods in Applied Mechanics and Engineering*, 126:17–38, 1995.
18. J. Fish and K. Shek. Multiscale analysis of composite materials and structures. *Composites Science and Technology*, 60:2547–2556, 2000.
19. J. Fish, K. Shek, M. Pandheeradi, and M. S. Shepard. Computational plasticity for composite structures based on mathematical homogenization: Theory and practice. *Computer Methods in Applied Mechanics and Engineering*, 148:53–73, 1997.
20. S. Ghosh and S. Moorthy. Elastic-plastic analysis of arbitrary heterogeneous materials with the Voronoi Cell finite element

- method. *Computer Methods in Applied Mechanics and Engineering*, 121, 1995.
21. S. Ghosh, K. Lee, and S. Moorthy. Multiple scale analysis of heterogeneous elastic structures using homogenization theory and Voronoi cell finite element method. *International Journal of Solids and Structures*, 32(1):27–62, 1995.
 22. S. Ghosh, K. Lee, and S. Moorthy. Two scale analysis of heterogeneous elastic-plastic materials with asymptotic homogenization and Voronoi cell finite element model. *Computer Methods in Applied Mechanics and Engineering*, 132:63–116, 1996.
 23. S. Ghosh, Y. Ling, B. Majumdar, and R. Kim. Interfacial debonding analysis in multiple fiber reinforced composites. *Mechanics of Materials*, 32:561–591, 2000.
 24. S. Ghosh, K. Lee, and P. Raghavan. A multi-level computational model for multi-scale damage analysis in composite and porous materials. *International Journal of Solids and Structures*, 2001.
 25. L. Girard, S. Bouillon, J. Weiss, D. Amitrano, T. Fichet, and V. Legat. A new modeling framework for sea-ice mechanics based on elasto-brittle rheology. *Annals of Glaciology*, 52(57):123–132, 2011.
 26. A. E. Green and P. M. Naghdi. A general theory of an elastic-plastic continuum. *Archive for Rational Mechanics and Analysis*, 18:251–281, 1965.
 27. W. Guo, H. Dong, M. Lu, and X. Zhao. The coupled effects of thickness and delamination on cracking resistance of X70 pipeline steel. *International Journal of Pressure Vessels and Piping*, 79:403–412, 2002.
 28. A. L. Gurson. Continuum theory of ductile rupture by void nucleation and growth: Part I – yield criteria and flow rules for porous ductile media. *Journal of Engineering Materials and Technology*, 99(1):2–15, 1977.
 29. M. W. Hernquist. Effects of crack arresting delaminations in Aluminum-Lithium alloys. Master's thesis, University of Illinois at Urbana-Champaign, 2010.
 30. W. M. Johnston, W. D. Pollock, and D. S. Dawicke. Biaxial testing of 2195 aluminum lithium alloy using cruciform specimens. Technical Report CR-2002-211942, NASA, 2002.
 31. L. M. Kachanov. On rupture time under creep conditions. *International Journal of Fracture*, 97:xi–xviii, 1999.
 32. P. Kanoute, D. P. Boso, J. L. Chaboche, and B. A. Schrefler. Multiscale methods for composites: A review. *Archive of Computational Methods in Engineering*, 16:31–75, 2009.
 33. R. D. Knutsen and R. Hutchings. Occurrence of non-metallic inclusions in 3CR12 steel and their effect on impact toughness. *Materials Science and Technology A*, 4:127–135, 1988.
 34. S. Kok, A. J. Beaudoin, and D. A. Tortorelli. A polycrystal plasticity model based on the mechanical threshold. *International Journal of Plasticity*, 18:715–741, 2002.
 35. K. Lee, S. Moorthy, and S. Ghosh. Multiple scale computational model for damage in composite materials. *Computer Methods in Applied Mechanics and Engineering*, 172:175–201, 1999.
 36. C. J. McMahon Jr. Hydrogen-induced intergranular fracture of steels. *Engineering Fracture Mechanics*, 68:731–788, 2001.
 37. M. C. Messner, A. J. Beaudoin, and R. H. Dodds. Mesoscopic modeling of crack arrestor delamination in Al-Li: Primary crack shielding and T -stress effect. *International Journal of Fracture*, 188:229–249, 2014.
 38. M. C. Messner, A. J. Beaudoin, and R. H. Dodds. Consistent crystal plasticity kinematics and linearization for the implicit finite element method. *Submitted for publication*, 2014.
 39. M. C. Messner, A. J. Beaudoin, and R. H. Dodds. An interface compatibility/equilibrium mechanism for delamination fracture in aluminum-lithium alloys. *Engineering Fracture Mechanics*, In press.
 40. T. Mura. *Micromechanics of defects in solids*. Martinus Nijhoff, 1991.
 41. I. A. Ovid'ko. Review on the fracture processes in nanocrystalline materials. *Journal of Materials Science*, 42:1694–1708, 2007.
 42. R. Raj. Intergranular fracture in bicrystals. *Acta Metallurgica*, 26:341–349, 1978.
 43. R. Raj and M. F. Ashby. Intergranular fracture at elevated temperature. *Acta Metallurgica*, 23:653–666, 1975.
 44. Y. R. Rashid. Ultimate strength analysis of prestressed concrete pressure vessels. *Nuclear Engineering and Design*, 7:334–344, 1968.
 45. A. Reuss. Berechnung der fließgrenze von mischkristallen auf grund der plastizitätsbedingung für einkristalle. *Zeitschrift für Angewandte Mathematik und Mechanik*, 9:49–58, 1929.
 46. J. R. Rice and D. M. Tracey. On the ductile enlargement of voids in triaxial stress fields. *Journal of the Mechanics and Physics of Solids*, 17:201–217, 1969.
 47. R. J. Rioja and J. Liu. The evolution of Al-Li base products for aerospace and space applications. *Metall Mater Trans A*, 43:3325–3337, 2012.
 48. J. J. Schutte. Fatigue crack propagation in 7050-T7451 plate alloy. *Engineering Fracture Mechanics*, 76:1037–1048, 2009.
 49. P. Scott. A review of irradiation assisted stress corrosion cracking. *Journal of Nuclear Materials*, 211:101–112, 1994.
 50. K. Tanaka and T. Mori. Note on volume integrals of the elastic field around an ellipsoidal inclusion. *Journal of Elasticity*, 2:199–200, 1972.
 51. W. Tayon. Personal communication, 2011.
 52. W. Tayon, R. Crooks, M. Domack, and J. Wagner. EBSD study of delamination fracture in Al-Li Alloy 2090. *Experimental Mechanics*, 50:135–143, 2010.
 53. V. Tvergaard and A. Needleman. Analysis of the cup-cone fracture in a round tensile bar. *Acta Metallurgica*, 32(1):157–169, 1984.
 54. D. C. Vander Kooi, W. Park, and M. R. Hilton. Characterization of cryogenic mechanical properties of Aluminum-Lithium alloy C-458. *Scripta Materialia*, 41:1185–1190, 1999.
 55. K. T. Venkateswara Rao and R. O. Ritchie. Mechanical properties of Al-Li alloys Part 1 fracture toughness and microstructure. *Materials Science and Technology*, 5:882–895, 1989.
 56. K. T. Venkateswara Rao and R. O. Ritchie. Fatigue of aluminum-lithium alloys. *International Materials Reviews*, 37(4):153–185, 1992.
 57. K. T. Venkateswara Rao, W. Yu, and R. O. Ritchie. Fatigue crack propagation in Aluminum-Lithium Alloy 2090: Part I. Long crack behavior. *Metallurgical and Materials Transactions A*, 19A:549–561, 1988.
 58. K. T. Venkateswara Rao, W. Yu, and R. O. Ritchie. Fatigue crack propagation in Aluminum-Lithium Alloy 2090: Part II. Small crack behavior. *Metallurgical and Materials Transactions A*, 19A:563–569, 1988.
 59. K. T. Venkateswara Rao, W. Yu, and R. O. Ritchie. On the behavior of small fatigue cracks in commercial aluminum-lithium alloys. *Engineering Fracture Mechanics*, 31:623–635, 1988.
 60. K. T. Venkateswara Rao, W. Yu, and R. O. Ritchie. Cryogenic toughness of commercial Aluminum-Lithium alloys: Role of delamination toughening. *Metallurgical Transactions A*, 20A:485–497, 1989.
 61. K. T. Venkateswara Rao, R. J. Bucci, K. V. Jata, and R. O. Ritchie. A comparison of fatigue-crack propagation behavior in sheet and plate aluminum-lithium alloys. *Materials Science and Engineering*, A141:39–48, 1991.

-
62. W. Voigt. Ueber die beziehung zwischen den beiden elastizitaetskonstanten isotroper koerper. *Annalen der Physik (Wiedemann)*, 38:573–587, 1889.
 63. C. L. White, R. A. Padgett, C. T. Liu, and S. M. Yalisove. Sucracking grain boundary segregation in relation to intergranular fracture: boron and sulfur in ni_3al . *Scripta Materialia*, 18:1714–1420, 1984.
 64. W. Yu and R. O. Ritchie. Fatigue crack propogation in 2090 Aluminum-Lithium alloy: effect of compression overload cycles. *Journal of Engineering Materials and Technology*, 109: 81–85, 1987.